Available online at www.sciencedirect.com
ScienceDirect
Trans. Nonferrous Met. Soc. China 32(2022) 1442−1459
Transactions of Nonferrous Metals Society of China
www.tnmsc.cn

Effect of Cr elimination on flow behavior and processing map of newly developed ECO-7175 aluminum alloy during hot compression

Majid SEYED-SALEHI[1], Bong Hwan KIM[2], Seung Yoon YANG[2,3], Shae Kwang KIM[2], Ghasem EISAABADI BOZCHALOEI[4]

1. Faculty of Materials Science and Engineering, K. N. Toosi University of Technology, 1969764499, Tehran, Iran;
2. Korea Institute of Industrial Technology, 7-47 Songdo-dong, Incheon 406-840, Korea;
3. Department of Advanced Materials Science and Engineering, Sungkyunkwan University, Suwon 16419, Korea;
4. Department of Materials Science and Engineering, Faculty of Engineering, Arak University, 3813853945, Arak, Iran

Received 3 May 2021; accepted 3 March 2022

Abstract: ECO-Al alloys are introduced as a game-changer for the aluminum industry and it is of utmost importance to determine the role of alloying elements in their processing characteristics. In this study, the effects of Cr on the hot deformation behavior of newly-developed ECO-7175 alloy were investigated. ECO-7175 samples with and without Cr were hot-compressed using a Gleeble simulator (temperature range of 350−500 °C and strain rates of 0.001−1 s^{-1}). The results were used to study the constitutive equations, the processing maps, and the microstructural evolution of the alloys. In Cr-containing alloy, the analysis of the deformation activation energy reveals that the rate-controlling mechanisms of the deformation change gradually from self-diffusion of Al (or diffusion of Mg in Al) to diffusion of Cr in Al by decreasing the Zener−Hollomon parameter. The analysis of the processing maps of Cr-containing alloy shows that the dynamic recrystallization (DRX) zone is limited to the deformation at high temperatures and low strain rates and expands with increasing applied strain. On the other hand, it is found that the self-diffusion of Al (or Mg in Al) is the only rate-controlling mechanism during hot deformation of Cr-free alloy in all processing conditions and its DRX zone is independent of the plastic strain.

Key words: hot deformation; constitutive equation; processing map; ECO-7175 aluminum alloy

1 Introduction

ECO-7175 is a variant of standard 7175 alloy made using ECO-Mg (Mg−Al_2Ca) instead of Mg during the manufacture of the alloys. The controlled oxidation of Mg during the casting of Al alloys in the ECO approach provides cleaner metal with fewer oxides and inclusions [1−3]. This also reduces the cost of production by minimizing the use of fluxes and expensive protective gases like SF_6 during melting and casting. The term "ECO" indicates that the alloy is environmentally friendly and more economical. Previous studies revealed that the cleanness of the melts during the casting of ECO-7175 alloy provides higher tensile properties and longer fatigue life than the standard 7175 alloy [1]. After casting, the ingots are generally subjected to a variety of thermo-mechanical processes (hot forging, rolling, or extrusion) that affect the microstructural characteristics and properties of the alloy [4]. Therefore, understanding the hot deformation behavior of this alloy is of great importance.

Evaluation of the hot deformation of Al−Zn−Mg−Cu alloys has been the subject of many studies [5−12]. Dynamic recovery (DRV) and the dynamic recrystallization (DRX) are reported as the

Corresponding author: Ghasem EISAABADI BOZCHALOEI, Tel: +98-9126847045, E-mail: g-eisaabadi@araku.ac.ir
DOI: 10.1016/S1003-6326(22)65885-0

main controlling mechanisms during the hot deformation of the 7xxx alloys. Although DRV is the main softening mechanism [10], it is reported that the decrease of strain rate and increase of deformation temperature transform the softening mechanisms from DRV to DRX [5,8,13]. Also, it is reported that the dynamic precipitation and/or coarsening during the hot deformation of 7xxx alloys leads to flow softening at deformation with a high value of the Zener−Hollomon parameter (Z) [6]. JIN et al [6] also showed that the decrease of Z causes more DRXed microstructure with coarser recrystallized grains. On the other hand, grain boundary sliding (GBS) can play a key role in the evolution of fine grains during hot compression of 7xxx aluminum alloy [14], as well as the appearance of super-plasticity during the hot deformation of an unrecrystallized coarse-grained 7475 alloy [15].

The kinetics of DRV and DRX significantly affects the flow behavior of alloys during hot deformation. The main constitutive models for the study of the deformation behavior of metallic materials can be categorized as phenomenological, physically-based and artificial neural network models [10]. A hyperbolic sine-type equation is frequently used for the description of the hot deformation behavior of 7xxx alloys [5,6,8,16]. It is reported that the peak stress of Al−Zn−Mg−Cu alloys decreases with the increase of deformation temperature [5,6] and decrease of the strain rate [6]. JIN et al [6] represented the peak stress of 7150 alloy by a hyperbolic-sine equation with an activation energy (Q) of 229.75 kJ/mol. The literature study [6,8,16] shows that the deformation activation energy of A1−Zn−Mg−Cu alloys depends on the presence of second phase particles and the solute drag effect. While the deformation activation energies of 141−162 and 143−156 kJ/mol are reported for aged and overaged 7012 and 7075 alloys, respectively [16], close to the self-diffusion activation energy of pure Al (142 kJ/mol), those of solution-treated 7012 and as-quenched 7075 alloys are 195−225 [16] and 256.6−300 kJ/mol [8,16], respectively.

The processing maps based on dynamic material model (DMM) are able to predict the microstructural evolution, deformation mechanisms and flow instability during hot deformation. LU et al [17] used isothermal uniaxial tension tests to find the hot deformation behavior and processing map of T6-7075 sheets and suggested that the temperature range of 300−407 °C and strain rates of 0.368−0.81 s^{-1} and also 422−450 °C and 0.05−1 s^{-1} are the optimum hot working conditions for the alloy. YANG et al [18] investigated the anisotropy of the hot flow behavior of extruded 7075 bars through hot-compression in different loading directions from the axis of the bars. They reported that regardless of loading angle, the optimum hot-working occurs at 480 °C and strain rate of 0.1 s^{-1}.

Alloying elements like Sc [19,20], Zr [19−21], and V [22] play key roles in the hot deformation behavior of 7xxx aluminum alloys. Our previous work [23], demonstrates that the elimination of Cr from the chemical composition of the ECO-7175 resulted in the removal of Zener pinning agents (Cr-rich ε precipitates ($Al_{18}Mg_3M_2$ (M=Sc, Ti, Cr, Mn, and Zr)) from the microstructure, which significantly affects the microstructure evolution during hot deformation. Since establishing a reliable constitutive model, processing map and determination of the softening mechanisms is of crucial importance for the new ECO 7175, in the present work, the effect of the elimination of Cr on the hot deformation behavior of this alloy is investigated through isothermal hot compression tests conducted within the temperature range of 350−500 °C and strain rate of 0.001−1 s^{-1}.

2 Experimental

In this study, two versions of as-extruded ECO-7175 alloy were used to investigate the effect of the elimination of Cr on the flow behavior, processing and instability maps. The chemical compositions of the examined alloys were determined by optical emission spectrometry (OES), as given in Table 1. Both Cr-containing and Cr-free ECO-7175 alloys contain a small amount of Al_2Ca [24] and were produced by direct chill (DC) casting of billets with a diameter of 127 mm. The billets were homogenized at 450 °C for 6 h and then extruded (extrusion temperature: 400 °C, extrusion ratio of 100:1, ram speed: 1 mm/s) to produce bars with a diameter of 12.7 mm. The bars were air cooled after extrusion.

The cylindrical specimens (H=15 mm and d=10 mm) were machined from the extruded bars.

Table 1 Chemical compositions of tested alloys (wt.%)

Element	ECO-7175 alloy	
	Cr-containing (CC)	Cr-free (CF)
Si	0.05	0.05
Fe	0.18	0.17
Cu	1.37	1.38
Mn	0.01	0.01
Mg	2.44	2.42
Cr	0.22	–
Zn	5.63	5.65
Ti	0.02	0.02
Ca	0.03	0.03
Al	Bal.	Bal.

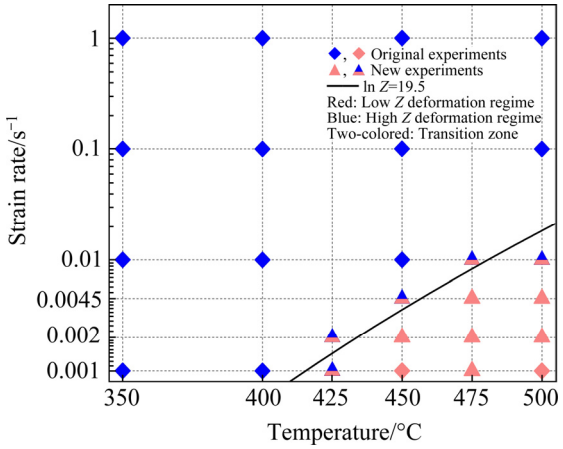

Fig. 1 Experimental conditions of hot compression tests

Uniaxial hot compression test was conducted by a Gleeble 3500 thermo-mechanical simulator at strain rates of 0.001−1 s^{-1} and temperatures of 300, 350, 400 and 450 °C to analyze the flow behavior of the alloys. Figure 1 schematically depicts the deformation condition (strain rates and temperatures) of the hot compression tests.

The samples were heated to the compression temperature at a heating rate of 10 °C/s, held for 3 min to provide homogeneous temperature distribution through the samples, deformed to the total true strain of 0.6 and finally quenched by high pressure cold air to the room temperature. Both sides of the hot compression test samples were lubricated by 0.25 mm-thick graphite film to minimize the friction between the sample and the tools. The temperature of test specimens was monitored during the test by a K-type thermocouple embedded inside the specimens. For this, a hole with a diameter of 0.6 mm and a depth of 3 mm was drilled at the mid-height of the specimens. The sequences of the hot compression test, specimen geometry and the position of the thermocouple are shown in Fig. 2.

After the compression tests, the samples were cut, ground and polished according to the standard metallography procedure. Then, the samples were electro-etched (with Barker's reagent: 200 mL of H_2O + 5 mL of HBF_4 and power supply of 20−25 V for 60−120 s) and the microstructure of the samples was studied by the polarized mode of Nikon MA200 optical microscope equipped with UPA polarization filter.

3 Results and discussion

3.1 Flow behavior

Figure 3 represents the true stress−strain curves of Cr-containing and Cr-free alloys compressed at 350, 400, 425, 450, 475 and 500 °C and strain rates of 0.001, 0.021, 0.0046, 0.01, 0.1

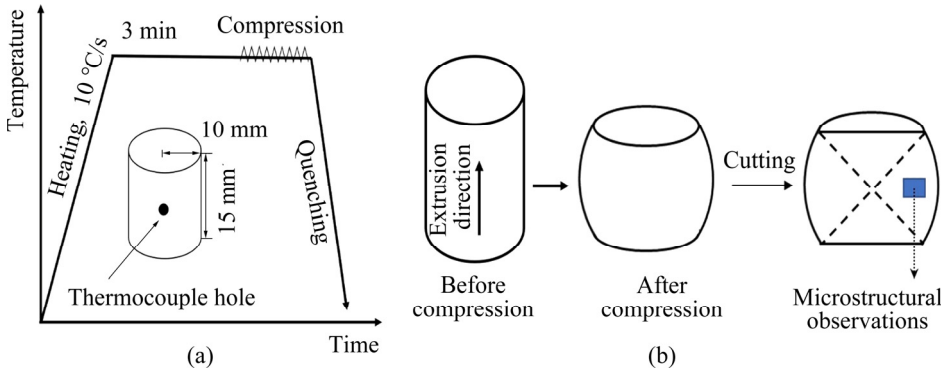

Fig. 2 Representation of hot compression testing sequences (a), and representation of dimensional change during hot compression and location of sampling for microstructural studies (b) [23]

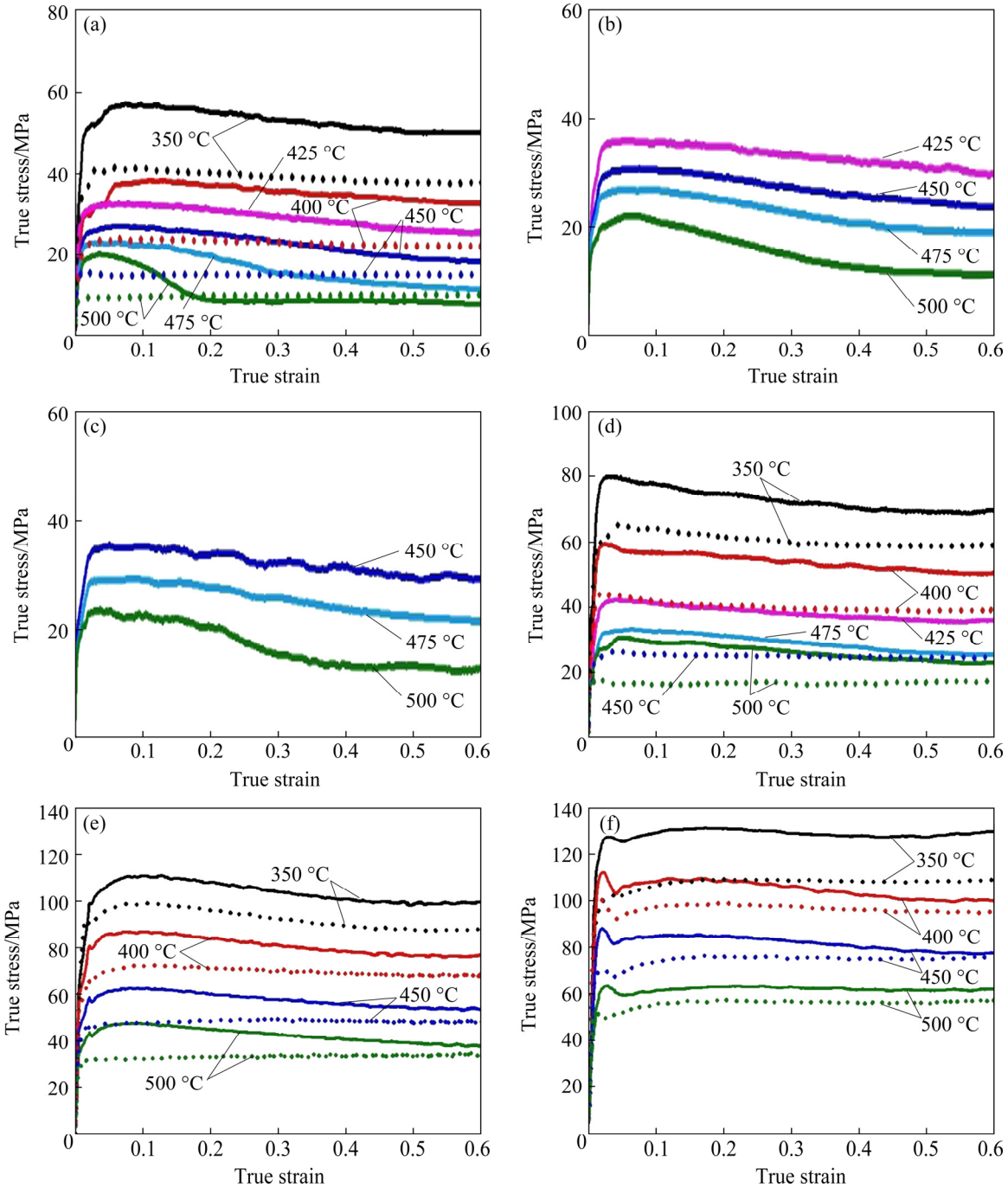

Fig. 3 True stress−strain curves of Cr-containing (solid lines) and Cr-free (dotted lines) ECO-7175 alloys deformed at different temperatures and strain rates: (a) 0.001 s^{-1}; (b) 0.0021 s^{-1}; (c) 0.0046 s^{-1}; (d) 0.01 s^{-1}; (e) 0.1 s^{-1}; (f) 1 s^{-1}

and 1 s^{-1}. The strain hardening and dynamic flow softening are the two competitive phenomena during hot deformation, which controls the flow behavior of the alloys. The two major controlling mechanisms in the hot deformation of aluminum alloys are DRX and DRV [25−28]. At the early stage of compression, the dramatic accumulation of dislocations and crystal defects contributes to a rapid increase in the flow stress [29,30], which is clear in Fig. 3. The accumulation of crystal defects increases the driving force of dynamic softening mechanisms and consequently increases the softening rate until the peak stress [30]. Subsequently, the flow stress reaches a steady-state (regardless of the test temperature and strain rate) when the rates of work hardening and dynamic softening (DRX and/or DRV) are almost the same [27,29,31−33]. Both the temperature and

strain rate have major impacts on the flow stress. At a given strain rate, the increase of the temperature (i.e., thermal activation) enhances the flow softening mechanisms and facilitates the dislocation slip mechanisms, and thus decreases the flow stress. Also, at a given temperature, the decrease of the strain rate decelerates the dislocation multiplication rate and extends the softening phenomena, and thus reduces the flow stress [5,6,30,31,34]. Also, it can be seen that the increase of deformation temperature and the decrease of strain rate, decrease the flow stress of both alloys. Figure 3 also reveals that the differences between the steady-state flow stresses of both alloys decrease with the increase of deformation temperature. Furthermore, in all test conditions, the flow stresses of Cr-containing samples are higher than those of Cr-free samples. This is probably due to the role of Cr in the solid solution strengthening (according to MURRAY [35], the solubility of Cr in Al increases from 0.02 to 0.1 at.% by increasing the temperature from 350 to 500 °C) and also the presence of uniformly dispersed fine ε-$Al_{18}Mg_3Cr_2$ particles that impede the movement of dislocations and increase the steady-state flow stress of the alloy by dispersion strengthening [21,23,28].

Microstructural examination of as-extruded Cr-containing and Cr-free alloys in our previous work [23] revealed elongated grains along the extrusion direction in both alloys. Also, the TEM equipped with energy-dispersive X-ray spectroscopy (EDS) and selected area electron diffraction (SAED) analysis exhibited the presence of Zn-rich η/η' ($Mg(Al,Zn)_2$, $Mg(Cu,Zn,Al)_2$, $Mg(Cu_xAl_{1-x})_2$) particles in the Al matrix in the alloys. The TEM analysis of as-extruded Cr-containing alloy reveals the α(Al) grains decorated by the platelets ε ($Al1_8Mg_3M_2$ (M=Sc, Ti, Cr, Mn and Zr) particles, and such particles are absent within the microstructure of the Cr-free alloy.

3.2 Constitutive model

The Sellars−Arrhenius constitutive equation (Eq. (1)) [36] is used to describe the relationship between the Zener−Hollomon parameter, Z, steady-state or peak stress, σ, of the alloys at elevated temperature:

$$Z = A[\sinh(\alpha\sigma)]^n \tag{1}$$

where A (s^{-1}), α (MPa^{-1}) and n are material constants and Z is expressed as [28]

$$Z = \dot{\varepsilon}\exp\left(\frac{Q}{RT}\right) \tag{2}$$

where $\dot{\varepsilon}$ (s^{-1}) is strain rate, T (K) is deformation temperature, Q (J/mol) is the apparent activation energy of deformation and R (=8.314 J/(mol·K)) is molar gas constant. The deformation activation energy reflects the difficulty of the hot deformation of the material [28,29]. Combining Eqs. (1) and (2) and taking the natural logarithm gives Eq. (3) for the deformation of metallic materials which can be simplified in Eq. (4):

$$\ln\dot{\varepsilon} + \frac{Q}{RT} = \ln A + n\ln[\sinh(\alpha\sigma)] \tag{3}$$

$$\ln\dot{\varepsilon} + \frac{Q}{RT} = \begin{cases} \ln A + n\ln[\sinh(\alpha\sigma)], \text{ for all } \alpha\sigma \\ \ln A' + n\ln\sigma, \text{ for low } \alpha\sigma \\ \ln A'' + \alpha'\sigma, \text{ for high } \alpha\sigma \end{cases} \tag{4}$$

where $A'=\alpha^n A$, $A''=A/2^n$ and $\alpha'=n\alpha$. The values of n and α' can be calculated by Eqs. (5) and (6), respectively:

$$n = (\partial\ln\dot{\varepsilon}/\partial\ln\sigma)_T \tag{5}$$

$$\alpha' = (\partial\ln\dot{\varepsilon}/\partial\sigma)_T \tag{6}$$

Therefore, the value of α can be calculated by Eq. (7):

$$\alpha = \left(\frac{\partial\ln\dot{\varepsilon}}{\partial\sigma}\right)_T \Big/ \left(\frac{\partial\ln\dot{\varepsilon}}{\partial\ln\sigma}\right)_T \tag{7}$$

At a given strain rate, Q is proportional to the slope of $\ln[\sinh(\alpha\sigma)]-1/T$ plot (Eq. (3)) and is given in Eq. (8) [30]:

$$Q = nR\left(\frac{\partial\ln[\sinh(\alpha\sigma)]}{\partial(1/T)}\right)_{\dot{\varepsilon}} \tag{8}$$

Alternatively, the combination of Eqs. (1) and (2) can also be written in the form of Eq. (9) (compared with Eq. (3)):

$$\ln\frac{[\sinh(\alpha\sigma)]^n}{\dot{\varepsilon}} = \frac{Q}{RT} - \ln A \tag{9}$$

From Eq. (9), the value of Q is also proportional to the slope of $\ln\{[\sinh(\alpha\sigma)]^n/\dot{\varepsilon}\}-1/T$ plot and can be calculated by Eq. (10):

$$Q = R\frac{\partial\left(\ln\{[\sinh(\alpha\sigma)]^n/\dot{\varepsilon}\}\right)}{\partial(1/T)} \tag{10}$$

It is of great importance to note that the calculation of Q by Eq. (8) involves taking

the average of the Q values determined for each $\dot{\varepsilon}$ [10,17,25,30,37−46]. However, Eq. (10) proposed in the present research gives a single Q value for all $\dot{\varepsilon}$ and does not require to take the average of Q values.

Finally, the value of A, can be determined by linear regression of Eq. (1) in the natural logarithm form ($\ln Z=\ln A+n\ln[\sinh(\alpha\sigma)]$), where $\ln Z=Q/(RT)+\ln\dot{\varepsilon}$.

According to Eq. (5), the average slope of the linear fitting of $\ln\dot{\varepsilon}-\ln\sigma$ plots at low stresses (where a linear relationship is observed) in Fig. 4(a) gives the value of n for Cr-free alloy (n_{CF}=4.74). Also, according to Eq. (6) the average of slope of the linear fitting of $\ln\dot{\varepsilon}-\sigma$ plots at high stresses with linear relationship in Fig. 4(b) gives the value of α' for Cr-free alloy (α'_{CF}=0.109). Thus, Eq. (7) gives $\alpha_{CF}=\alpha'_{CF}/n_{CF}$=0.023 MPa^{-1}.

The $\ln\dot{\varepsilon}-\ln\sigma$ and $\ln\dot{\varepsilon}-\sigma$ plots of the Cr-containing samples are presented in Fig. 5. From Fig. 5(a), while the $\ln\dot{\varepsilon}-\ln\sigma$ data from 350 and 400 °C can be described by a single fitted line, the data correspond to 450 and 500 °C are more accurately described by two fitted lines. Since the slopes of fitted lines in Fig. 5(a) represent the stress exponent, n, it seems that at temperatures higher than 400 °C and strain rate less than 0.01 s^{-1}, the deformation mechanism of the Cr-containing alloys is changed. The precise evaluation of the changes in the deformation mechanism is studied by adding eight new conditions (the triangles in Fig. 1) and will be discussed later. From Fig. 5(a), it is clear that there are two different deformation mechanisms with different stress exponents n, where at low temperatures and high strain rates (1st deformation regime) n_{CC}=4.30 and otherwise (2nd deformation regime) n_{CC}=2.07. Furthermore, the slope of $\ln\dot{\varepsilon}-\sigma$ plots in Fig. 5(b) gives α'_{CC}=0.122. Therefore, $\alpha_{CC,1st\ regime}$ =0.018 MPa^{-1} and $\alpha_{CC,\ 2nd\ regime}$ = 0.059 MPa^{-1}.

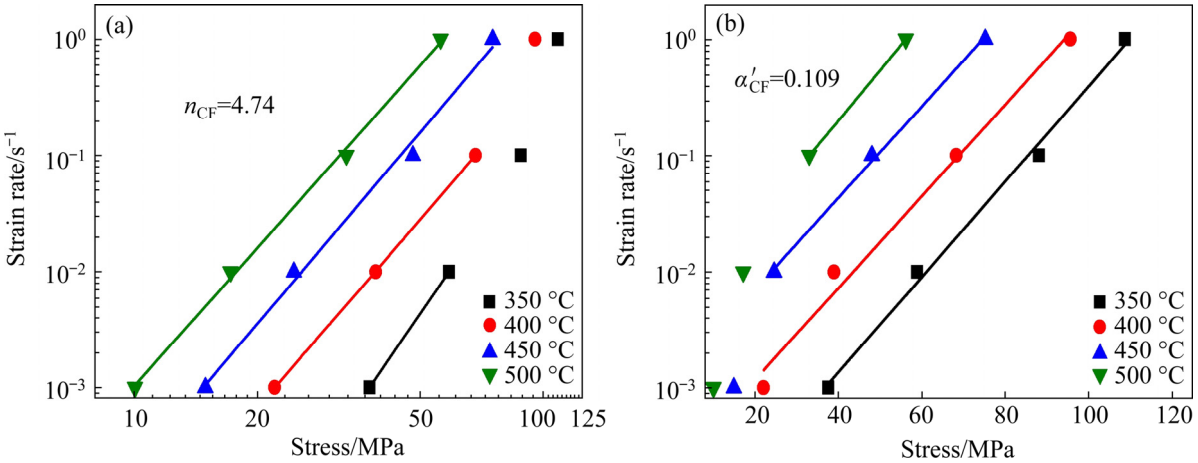

Fig. 4 Relationships between strain rates and steady-state stress values for Cr-free alloy: (a) $\ln\dot{\varepsilon}-\ln\sigma$; (b) $\ln\dot{\varepsilon}-\sigma$

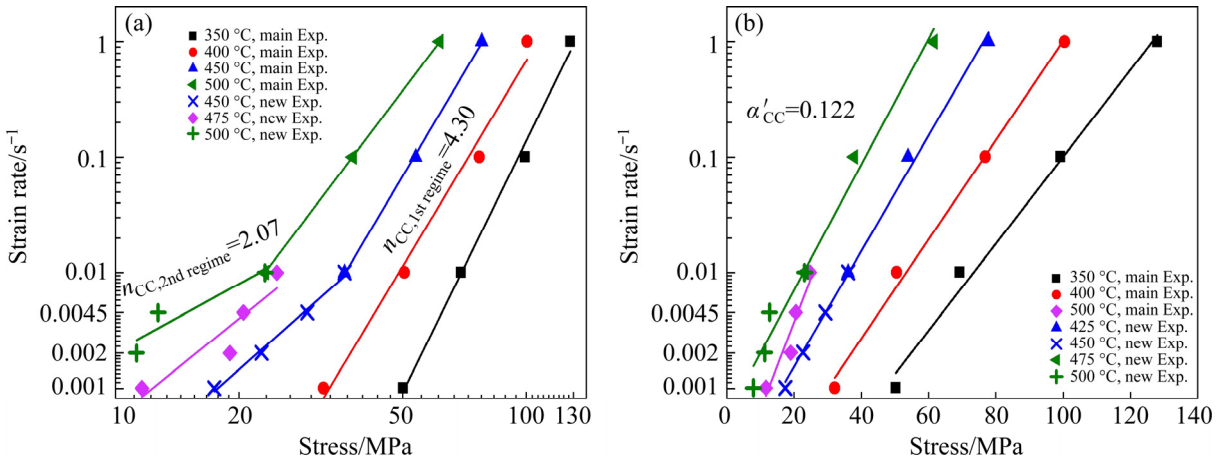

Fig. 5 Relationships between strain rates and steady-state stress values for Cr-containing alloy: (a) $\ln\dot{\varepsilon}-\ln\sigma$; (b) $\ln\dot{\varepsilon}-\sigma$

According to Eq. (10) the activation energy, Q, is the linear proportion factor of $\ln\{[\sinh(\alpha\sigma)]^n/\dot{\varepsilon}\}$ vs $1/T$ multiplied by molar gas constant, R. The $\ln\{[\sinh(\alpha\sigma)]^n/\dot{\varepsilon}\}$ vs temperature plot in Fig. 6(a) gives the apparent activation energy of 130.5 kJ/mol for Cr-free alloy which is close to the activation energy of lattice self-diffusion of pure Al (142 kJ/mol) [18], diffusion of Mg in Al (120.5−130.4 kJ/mol) [47] and Zn in Al (116.1−121.4 kJ/mol) [47]. Figures 6(b, c) show the $\ln\{[\sinh(\alpha\sigma)]^n/\dot{\varepsilon}\}$ vs reciprocal temperature plots of the Cr-containing alloy by using the materials constants (n and α) obtained for the first and second deformation regimes, respectively (see Fig. 5). In Fig. 6(b), the data points of the first deformation regime follow a linear relationship, while the data points of the second deformation regime deviate from the linear relationship. Similarly, the data points of the second deformation regime in Fig. 6(c) follow a linear relationship, while the data points of the first deformation regime show a deviation from the fitted line. The slopes of the fitted lines in Figs. 6(b, c) give the apparent activation energy of 152.3 and 180.7 kJ/mol for the first and second deformation regimes, respectively. The apparent activation energy of the Cr-containing alloy in the 1st regime (152.3 kJ/mol) is close to that of lattice self-diffusion of pure Al (142 kJ/mol) [18]. Therefore, it is reasonable to conclude that in the 1st regime (high Z, high strain rates and low temperatures), the dominant rate-controlling mechanism of the alloy is the lattice self-diffusion. On the other hand, in the 2nd regime (low Z, low strain rates and high temperatures), the considerably higher apparent activation energy of the Cr-containing alloy suggests that the lattice self-diffusion of Al is not the dominant rate-controlling mechanism. According to our previous study [23], the presence of minor amounts of Cr in the chemical composition of ECO-7175 alloy results in the formation of Cr-rich ε precipitates that act as Zener pining agents at low temperature and inhibit the SRX and DRX during hot deformation. However, according to the thermodynamic modeling of the equilibrium phases of 7175 alloy in Ref. [23], by increasing the temperature above 400 °C, the ε precipitates start to dissolve, which in turn decreases the effect of Zener drag. Since the dissolution of ε precipitates is a diffusional process, lower strain rates of hot deformation increase the extent of dissolution (by providing longer time), which increases the concentration of the Cr solved in the Al matrix. The diffusion of solute atoms (Cr) into the dislocations (the solute atmosphere at the vicinity of dislocations) increases the lattice friction and retards the movement of dislocations by slip mechanisms or thermally activated recovery [6,48], which increases the energy required for dislocation movement [6,48,49]. Also, the segregation of solute atoms into the grain boundaries can effectively decrease the grain boundary movement during recrystallization by exerting a drag force [50] and change the kinetics of DRX. In these circumstances,

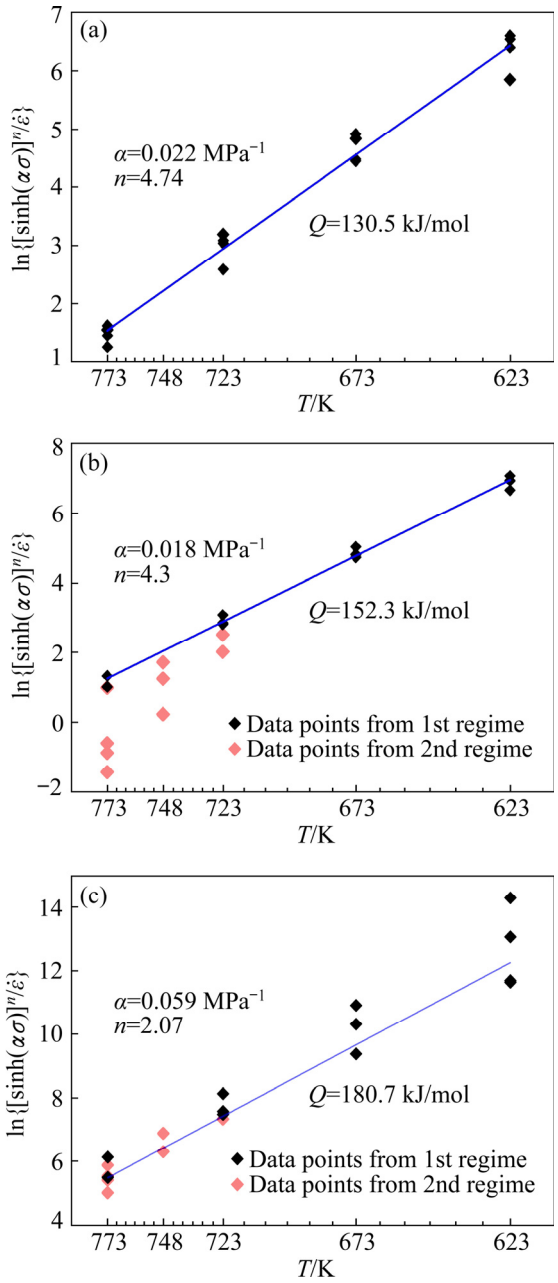

Fig. 6 $\ln\{[\sinh(\alpha\sigma)]^n/\dot{\varepsilon}\}$ vs temperature (from Eq. (10)) plots of Cr-free (a), and Cr-containing (b, c) ECO-7175

the activation energy of grain boundary movement is a complicated quantity and depends on the solute concentration, temperature and grain boundary velocity [51]. It is very well known [52,53] that the presence of alloying elements changes the activation energy of the grain boundary movement. Hence, the activation energy of the grain boundary movement would be between the activation energy of the grain boundary self-diffusion of the base metal (142 kJ/mol for Al) and that of diffusion of the solute atoms (261.9 kJ/mol for diffusion of Cr in Al [54]) [50,51]. Therefore, the apparent activation energy of 180.7 kJ/mol suggests that the diffusion of Cr in Al is the rate-controlling mechanisms during the hot deformation of Cr-containing alloy in low Z regime (2nd deformation regime).

Taking natural logarithm from both sides of Eq. (1) gives

$$\ln Z = \ln A + n \ln[\sinh(\alpha\sigma)] \quad (11)$$

Therefore, the values of $\ln A$ and n are the intercept and slope of the fitted line in $\ln Z$ vs $\ln[\sinh(\alpha\sigma)]$ plots in Fig. 7. The fitted lines in Figs. 7(b, c) also show the linear relationship of the data points from high and low Z regimes, respectively.

The classification of different hot deformation tests by their rate-controlling mechanisms is depicted in Fig. 1. As discussed in the previous section, while most of the deformation conditions fall in the 1st deformation regime in which the self-diffusion of Al (or diffusion of Mg in Al matrix) is the rate-controlling mechanisms of the hot deformation, at low strain rates and higher temperature, the diffusion of Cr in Al matrix is the rate-controlling mechanism. Also, the transition between the 1st and the 2nd regimes is represented by a hypothetical line ($\ln Z$=19.5). In other words, the 1st deformation mechanism is dominant at high values of Z ($\ln Z$>19.5) and the 2nd deformation mechanism is dominant at low values of Z ($\ln Z$<19.5).

The values of material constants of the examined alloys are summarized in Table 2. The values in this table are used for prediction of the steady-state stress of the examined alloys. The comparison of the predicted and experimental steady-state stress values is presented in Fig. 8 and it is revealed that the proposed equations (based on

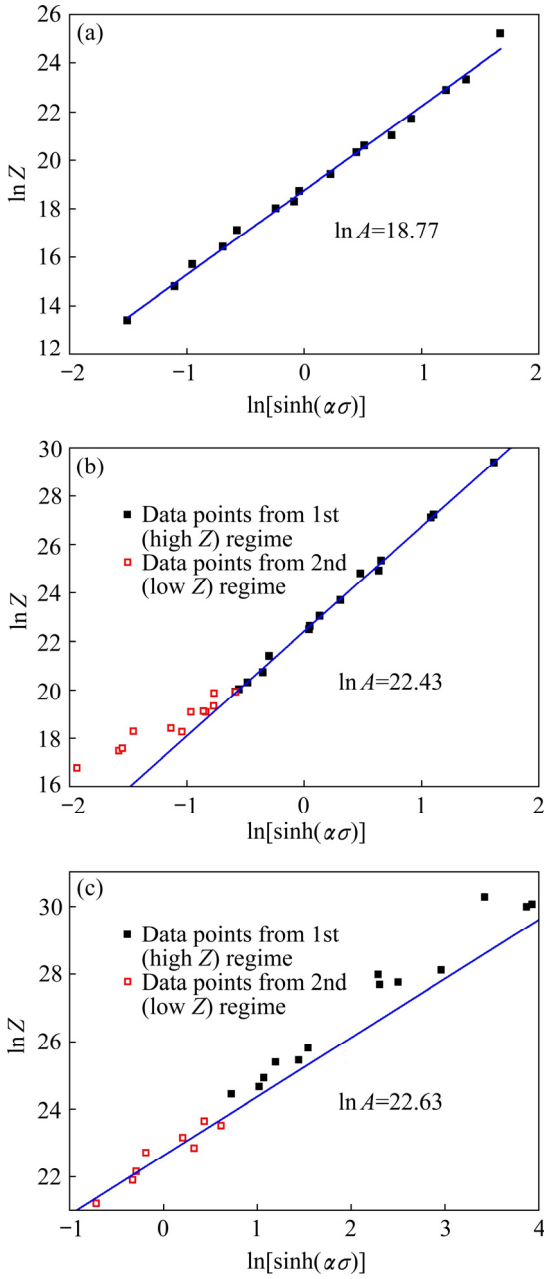

Fig. 7 Relationships between Zener−Hollomon parameter and steady-state stress, i.e., $\ln Z$ vs $\ln[\sinh(\alpha\sigma)]$, for Cr-free (a), and Cr-containing (b, c) alloys

Table 2 Material constants for Cr-fee and Cr-containing alloys used for prediction of steady-state stress

Constant	Cr-containing alloy		Cr-free alloy
	1st (high Z) regime	2nd (low Z) regime	
n	4.30	2.07	4.74
α/MPa^{-1}	0.018	0.059	0.022
Q/(kJ·mol^{-1})	152.3	180.7	130.5
$\ln A$	22.43	22.63	18.77

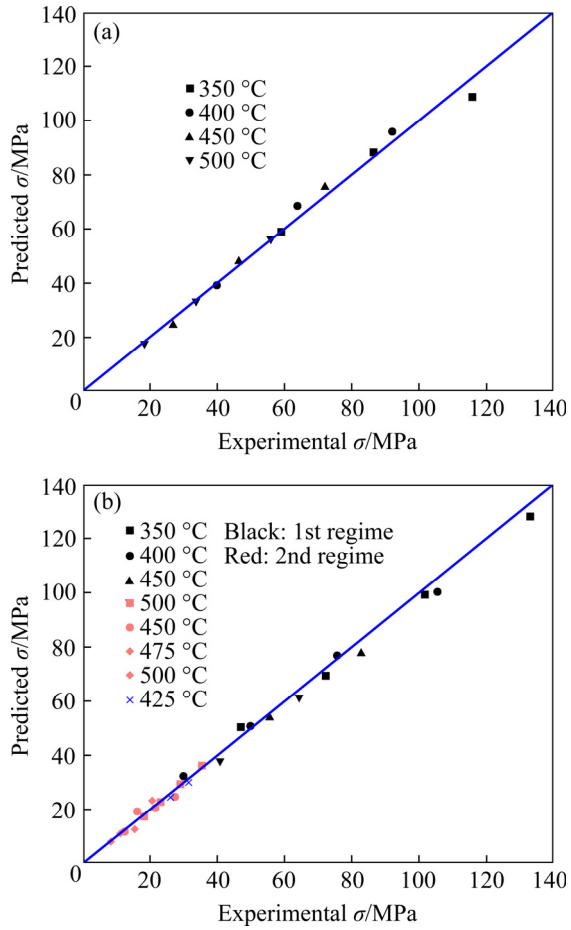

Fig. 8 Predicted vs experimental values of steady-state flow stress for Cr-free (a) and Cr-containing (b) ECO-7175 alloys

the calculated material constants) predict the steady-state flow stress of the alloy with very good accuracy.

The standard Arrhenius plots of σ (in logarithmic scale) vs temperature may be used to simply derive the apparent activation energy of deformation which is employed for Cr-containing alloy, at different strains and strain rate of 0.001 s^{-1} (shown in Fig. 9). The plots in Fig. 9 exhibit two different kinetic rates for low (≤425 °C) and high temperature (≥425 °C) deformations. At low-temperature deformation, the fitted lines of different strains are almost parallel and show similar apparent activation energy (line slopes). On the other hand, at high-temperature deformation, the slopes (i.e., the apparent activation energy) of the fitted line at low strain are considerably different from the slope of the fitted lines at high strain (ε=0.2, 0.3, 0.4, 0.5, 0.6 and steady-state strain). From Fig. 9, it can be seen that the fitted line for peak strain at high temperature is parallel to the fitted lines of the low-temperature regime, which indicates a similar kinetic rate equation with the same apparent activation energy. Also, it can be seen that at the high-temperature deformation, the activation energy is increased by applying further strain. This indicates that in the high-temperature regime, the deformation mechanism is gradually changed by increasing the strain. The gradual increase of the apparent activation energy at high temperatures and lower strain rates can be explained through the fact that applying plastic strain at low strain rates provides enough time for the diffusional dissolution of ε precipitates that promote the solute drag effects. To apply a given strain, a period of time elapses and at this time the solute drag mechanisms would be activated. In fact, applying more strain with elapsing more time, the more the dissolution of the precipitates is, the stronger the solute drag effect is. This explains the increase of the apparent activation energy with the increase of the strain.

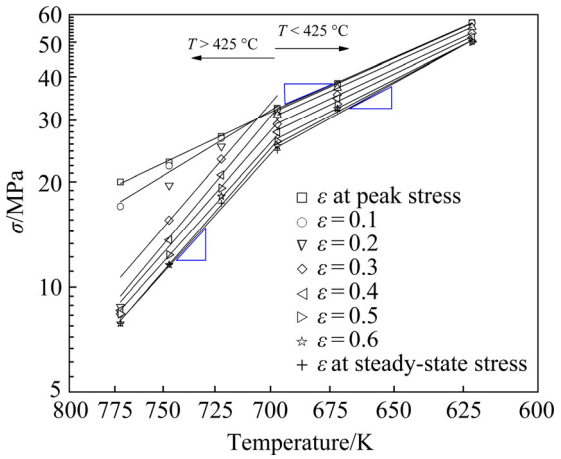

Fig. 9 Standard Arrhenius plot of σ vs temperature for Cr-containing alloy at $\dot{\varepsilon}$ =0.001 s^{-1} and ε=0.1, 0.2, 0.3, 0.4, 0.5, 0.6, at peak stress and peak strain

3.3 Processing maps

The principles of DMM were used to construct the 3D processing maps for the evaluation of the hot deformation behavior and workability of the examined alloys. In DMM, the instantaneous total power dissipated during deformation (P) is divided into two complementary parts, i.e., G (temperature-related or power dissipated by plastic work) and J (microstructure-related or microstructural evolution mechanisms that dynamically dissipate power) [55] according to Eq. (12):

$$P=\sigma\dot{\varepsilon}=G+J=\int_0^{\dot{\varepsilon}}\sigma \mathrm{d}\dot{\varepsilon}+\int_0^{\sigma}\dot{\varepsilon}\mathrm{d}\sigma \tag{12}$$

where σ and ε are flow stress, and true strain, respectively.

For a given strain and deformation temperature, the flow stress can be expressed as

$$\sigma=k\dot{\varepsilon}^{m(\dot{\varepsilon},T,\varepsilon)} \tag{13}$$

where k is a material constant and m is strain rate sensitivity index and can be expressed by

$$m=\frac{\partial J}{\partial G}=\frac{\partial(\ln\sigma)}{\partial(\ln\dot{\varepsilon})}\approx\frac{\Delta\ln\sigma}{\Delta\ln\dot{\varepsilon}} \tag{14}$$

Consequently, the value of J can be derived as

$$J=\int_0^{\sigma}\dot{\varepsilon}\mathrm{d}\sigma=\frac{m\sigma\dot{\varepsilon}}{m+1} \tag{15}$$

where m (=1) represents an ideal dissipation state and results in $J_{\max}=\sigma\dot{\varepsilon}/2$. Accordingly, the efficiency of power dissipation of material, η, can be written as [29]

$$\eta(T,\varepsilon,\dot{\varepsilon})=\frac{J}{J_{\max}}=\frac{2m}{m+1} \tag{16}$$

Furthermore, according to the extreme principle of irreversible thermodynamics proposed by ZIEGLER [56], the flow instability (dimensionless parameter ξ), is defined as

$$\xi(\dot{\varepsilon})=\frac{\partial\ln\left(\frac{m}{m+1}\right)}{\partial\ln\dot{\varepsilon}}+m<0 \tag{17}$$

where the distribution of m is obtained by a numerical differentiating based on Eq. (14) and then, the values of η and ξ can be calculated by Eqs. (16) and (17).

The 3D power dissipation and flow instability maps of examined alloys are presented in Fig. 10, in which 350 °C ≤ T ≤ 500 °C, 0.1 ≤ ε ≤ 0.6, and 0.001 s^{-1}≤ $\dot{\varepsilon}$ ≤ 1 s^{-1}. In Figs. 10(a, b), the regions with high η represent the conditions that lead to the good workability of the examined alloys [15,57,58]. However, it should be noted that the area with the high η does not necessarily guaranty the ideal workability due to the occurrence of local flow instability [15,57] associated with adiabatic shear bands, deformation bands and flow localization [59]. Furthermore, the regions with high η also represent the conditions that may lead to the microstructural evolution such as DRV, DRX [60,61], and superplasticity [59,62,63]. It is reported [62,63] that the efficiency (η) of DRX and DRV is 20%−30% and 35%−45%, respectively. According to PRASAD [59], the typical microstructural evolution mechanisms, such as DRV and DRX, can be determined by η values. Figures 10(c, d) represent the processing condition under which the deformation of the examined alloys is predicted to be unstable (i.e., ξ < 0). In this condition, the flow localization, adiabatic shear banding, or cracking may occur and lead to the formation of inhomogeneous defect-containing microstructure during hot working. Therefore, this regime should be avoided in designing a hot working process [58].

For the Cr-containing alloy (Fig. 10(a)), the domain with the high power dissipation efficiency (η≥30%) [64] occurs at low strain rates (0.001−0.01 s^{-1}) and high temperatures (>425 °C). It can be seen that η distribution of the Cr-free alloy in Fig. 10(b) is basically similar to that of the Cr-containing alloy in Fig. 10(a). However, the domain associated with η≥30% is larger for the Cr-free alloy. Therefore, it can be concluded that the microstructure of Cr-free alloy evolves by DRX in all processing conditions except those with low temperature (<400 °C) and high strain rate (>0.1 s^{-1}). Comparison of Figs. 10(c) with 10(d) reveals that high strain rates (>0.1 s^{-1}) and low temperatures (<400 °C) results in flow instability in both alloys. However, the increase of the strain decreases the severity of flow instability.

A closer examination of the power dissipation efficiency and flow instability is conducted by sectioning and combining the 3D η and ξ maps of the examined alloys at ε=0.1−0.6 and the results are presented in Figs. 11 and 12. Both figures reveal the presence of triangular-shaped regions at high temperatures and low strain rates at which the DRX could occur (regions with η>0.3).

By comparing Figs. 11 with 12, it is clear that the DRX region in Cr-free alloy is larger than that in Cr-containing alloy. In fact, Fig. 12 shows that except a triangular-shaped region located at high strain rates and low temperatures, DRX occurs at all deformation states and strains. Also, it can be concluded that the DRX region of Cr-free alloy is independent of the strain. On the other hand, comparison of Figs. 11(a−f) shows that the increase of the plastic strain enlarges the triangular-shaped

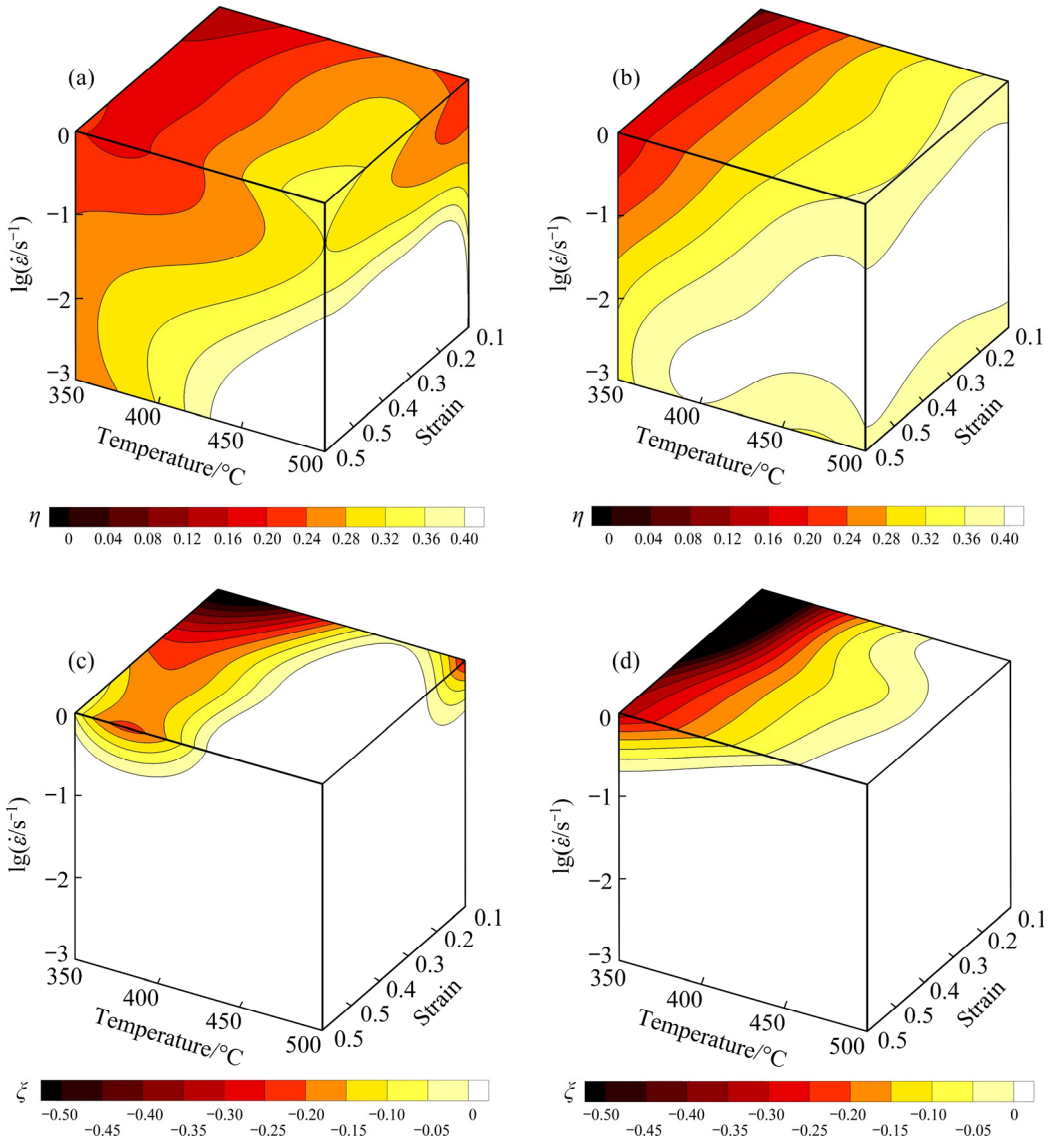

Fig. 10 3D power dissipation maps of Cr-containing (a) and Cr-free (b) alloys, and 3D instability maps of Cr-containing (c) and Cr-free (d) alloys

DRX region in Cr-containing alloy. Outside this region, DRX does not occur and it seems that this is due to the presence of Cr-rich ε precipitates that can cause Zener drag [23,65−67].

According to our previous study [23], the dissolution of ε precipitates above 425 °C may encourage the DRX in the Cr-containing alloy. Since the dissolution of the Cr-rich ε precipitates requires time due to its diffusional nature, the deformation at low strain rates (longer time to reach a specific strain) provides the time required for the dissolution of precipitates. On the other hand, the dissolution of precipitates at higher strain rates (shorter period of time) requires a larger thermal activation and therefore, higher temperatures.

Figure 11 shows that at the beginning of the deformation, the ε precipitates are not fully dissolved due to the time limitation, which makes the DRX less favorable at small strains. However, continually applying the plastic strain for a longer period of time (higher strains) escalates the dissolution of the precipitates and reduces the Zener drag effect. In other words, it can be seen from Fig. 11 that the increase of the applied strain expands the DRX region and the processing map of Cr-containing alloy highly depends on the strain.

These findings are in accordance with our previous study related to the effect of Cr elimination on the microstructure evolution at high temperatures [23]. Figures 13 and 14 show the

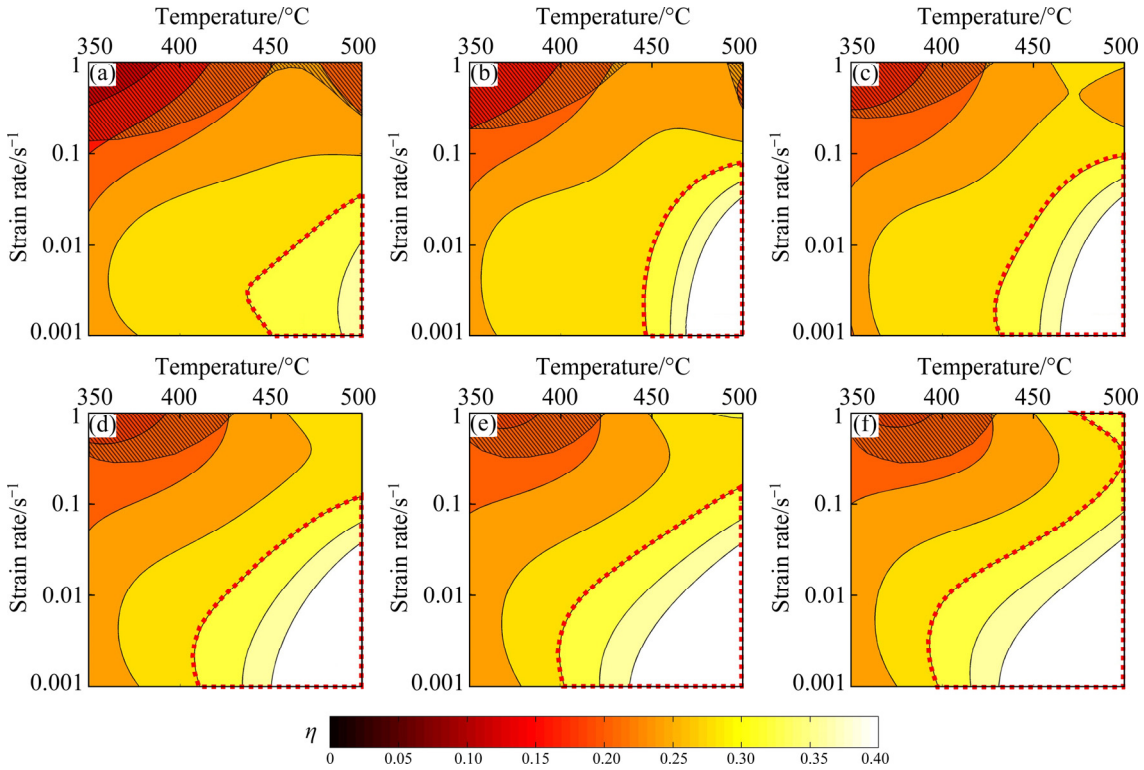

Fig. 11 Processing maps of Cr-containing alloy at true strain of 0.1 (a), 0.2 (b), 0.3 (c), 0.4 (d), 0.5 (e) and 0.6 (f) (The gray hatched area shows the instability region (i.e., $\xi<0$) and the area inside the dotted red lines show the DRX prone region (η>30%))

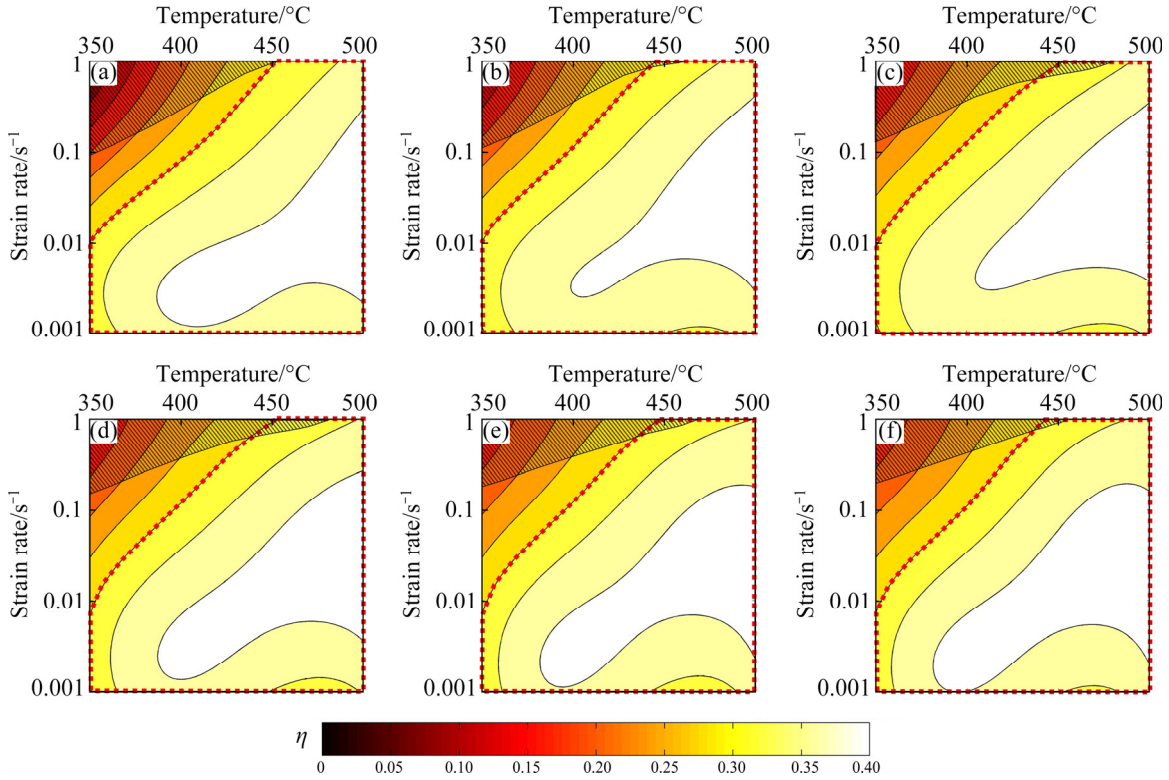

Fig. 12 Processing maps of Cr-free alloy at true strain of 0.1 (a), 0.2 (b), 0.3 (c), 0.4 (d), 0.5 (e) and 0.6 (f) (The gray hatched area shows the instability region (i.e., $\xi<0$) and the area inside the dotted red lines show the DRX prone region (η>30%))

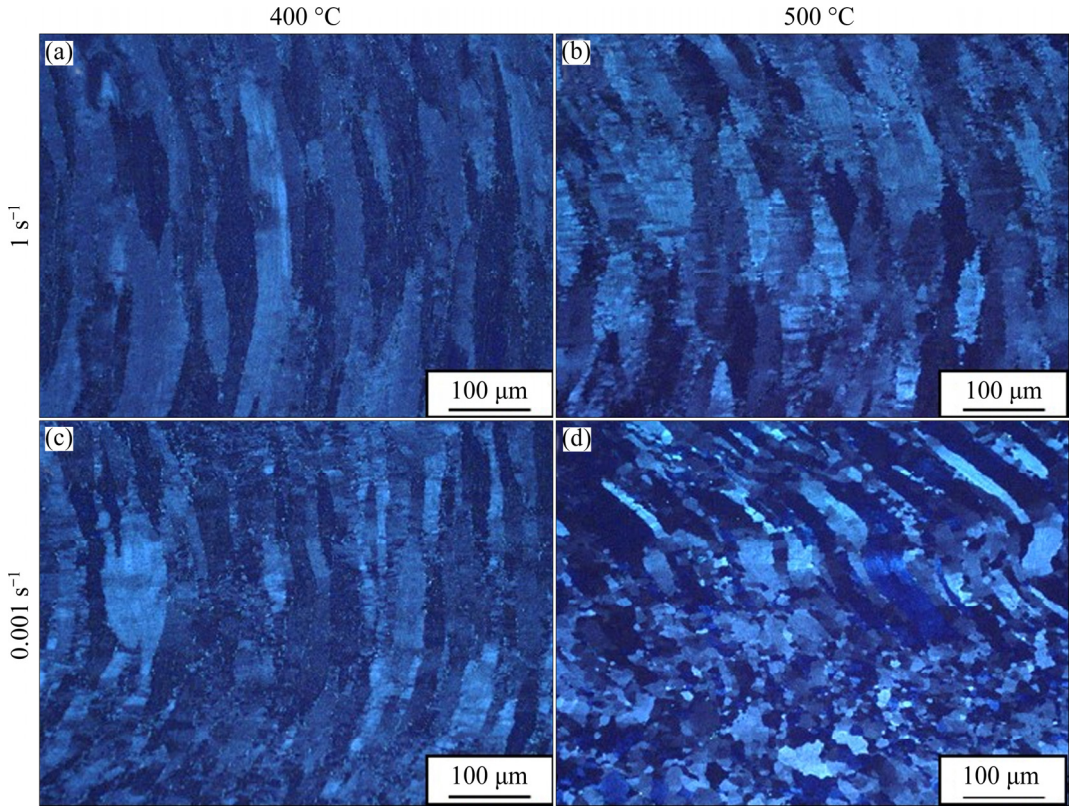

Fig. 13 Effects of hot deformation temperature and strain rate on microstructure of Cr-containing alloy [23]: (a) 400 °C and 1 s^{-1}; (b) 500 °C and 1 s^{-1}; (c) 400 °C and 0.001 s^{-1}; (d) 500 °C and 0.001 s^{-1}

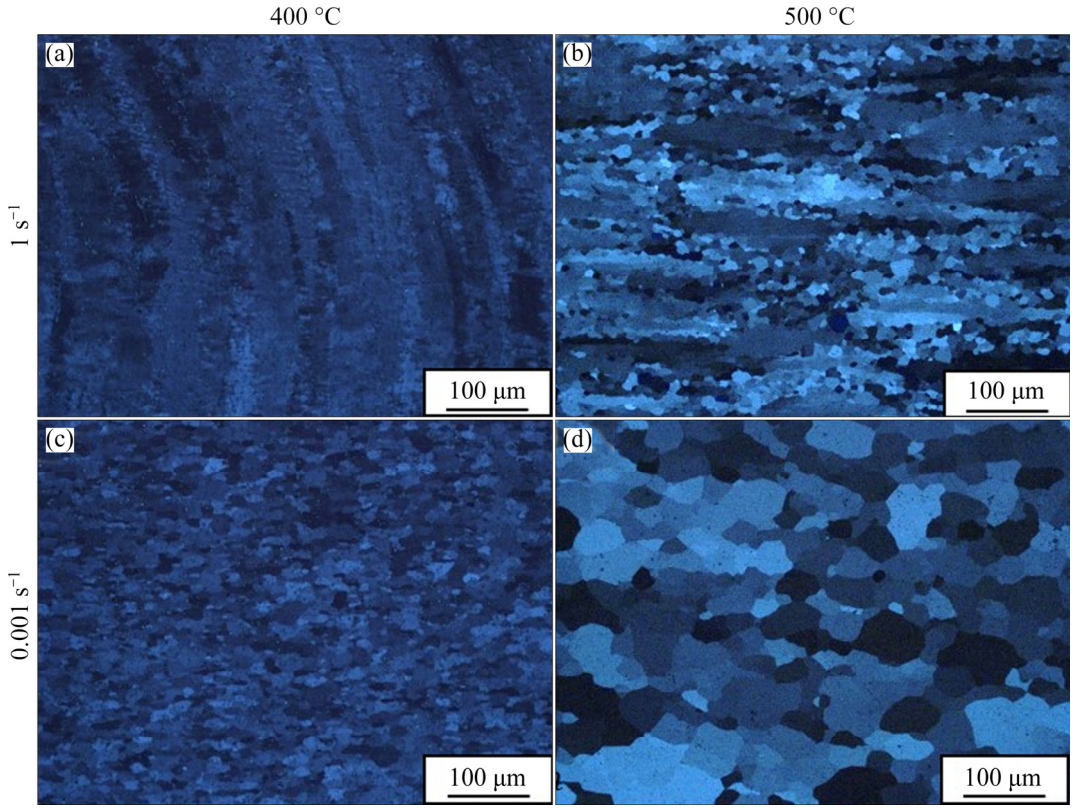

Fig. 14 Effects of hot deformation temperature and strain rate on microstructure of Cr-free alloy [23]: (a) 400 °C and 1 s^{-1}; (b) 500 °C and 1 s^{-1}; (c) 400 °C and 0.001 s^{-1}; (d) 500 °C and 0.001 s^{-1}

microstructure of Cr-containing and Cr-free alloys after hot deformation (at 400 and 500 °C and strain rates of 0.001 and 1 s^{-1}), respectively. From Fig. 13(a), it is clear that the hot deformation of Cr-containing alloy at 400 °C and strain rate of 1 s^{-1} did not result in DRX and the sample has retained its original as-deformed microstructure. Comparison of the micrographs in Fig. 13 shows that the increase of the hot deformation temperature and/or decrease of the strain rate increased the tendency for DRX in a way that the sample deformed at 500 °C and strain rates of 0.001 s^{-1} shows the features of partial DRX. On the other hand, the micrograph of Cr-free sample deformed at low temperature and high strain rate (400 °C and 1 s^{-1}) in Fig. 14(a) shows the original as-extruded microstructure along with fine DRXed grains. Similar to Cr-containing alloy, the increase of temperature and/or decrease of strain rate increased the tendency for DRX and a fully recrystallized microstructure of the Cr-free sample deformed at 500 °C and strain rate of 0.001 s^{-1} is presented in Fig. 14(d). In general, the Cr-free alloy shows a higher tendency for DRX than the Cr-containing one due to the elimination of second phase precipitates by removal of Cr from its chemical composition. As discussed previously [23], these precipitates act as Zener pining agents and prevent DRX. However, it must be noticed that the hot deformation of the Cr-containing alloy at high temperatures (higher than dissolution temperature of Cr-containing precipitates, 425 °C) and low strain rates (that provide the required time for precipitates dissolution) facilitates the way for recrystallization of this alloy. The occurrence of the DRX and its dependency on temperature and strain rate is predictable from the processing maps of examined alloys. In Fig. 12, there is a large DRX zone (η>30%) for Cr-free alloy at all processing conditions except those with low temperatures and high strain rates. However, the relatively small DRX zone of the Cr-containing alloy is limited to high temperatures and low strain rates. Therefore, there is a very good agreement between the processing maps of the examined alloys (Figs. 11 and 12) and their corresponding microstructure (Figs. 13 and 14). In Cr-containing alloy, the DRX zone is extended with the increase of the applied strain. In fact, at temperatures higher than the dissolution of Cr-containing precipitates (425 °C), the increase of the applied strain provides enough time for precipitates dissolution, which in turn encourages the DRX and extends the DRX zone in the processing map. As shown in Fig. 9, the dissolution of Cr-containing precipitates at higher temperatures changes the activation energy. In other words, the increase of applied strain facilitates the dissolution kinetics of Cr-containing precipitates. This phenomenon diminishes the Zener effect and encourages the DRX and results in the change of rate-controlling diffusional mechanisms due to the release of Cr atoms within the matrix.

4 Conclusions

(1) The hyperbolic sine constitutive equation can successfully describe the hot deformation behavior of the Cr-free alloy. The calculated activation energy of this alloy is comparable to the activation energy for the self-diffusion of Al or diffusion of Mg in Al matrix.

(2) The flow behavior of Cr-containing alloy is described by a bimodal hyperbolic sine constitutive equation whereas the activation energies of the deformation with low and high Zener−Hollomon parameters (Z) are 180.7 and 152.3 kJ/mol, respectively. It is found that the self-diffusion of Al or diffusion of Mg in Al matrix is the rate-controlling mechanism at high Z deformations. However, it seems that the rate-controlling mechanism at low Z is the diffusion of Cr in Al matrix.

(3) In Cr-containing alloy, the Cr-rich precipitates act as Zener pining agents and prevent DRX. At temperatures higher than the dissolution temperature of Cr-containing precipitates and low strain rates, the dissolution of the precipitates promotes the DRX. Comparison of the processing maps of examined alloys shows that the elimination of the Cr extends the DRX region. On the other hand, by dissolving the Cr-containing precipitates, the solute Cr atoms develop a solute drag effect that changes the rate-controlling mechanisms of hot deformation from the 1st to the 2nd regime.

(4) The processing map of Cr-containing alloy shows a strong dependency of power dissipation parameter to the strain. On the other hand, the power dissipation parameter of Cr-free alloy shows a weak dependency on the strain. In hot deformation of Cr-containing at high temperatures

(higher than the dissolution temperature of Cr-containing precipitates), the kinetics of Cr-rich precipitates dissolution progresses with the increase of applied plastic strain and elapsed time. The precipitates dissolution with increased strain encourages the DRX and extends the DRX zone in the processing map.

Acknowledgments

The authors would like to express their appreciation to the ECO Metal Team at Korea Institute of Industrial Technology for their collaborations for conducting the experiments.

References

[1] VU C. Fatigue characteristics of new ECO series aluminum 7175 alloy [D]. Department of Mechanical and Materials Engineering, Portland State University, Portland, USA, 2019. https://doi.org/10.15760/etd.6861.

[2] KIM S H, KIM K S, KIM S K, YOON Y O, CHOI K S, LEE K A. Microstructure and mechanical properties of ECO-2024-T3 aluminum alloy [J]. Advanced Materials Research, 2012, 602/603/604: 623−626. https://doi.org/10.4028/www.scientific.net/AMR.602-604.623.

[3] YEOM G Y, EISAABADI G, KIM S K, HYUN S K, SIM K S, YOON Y O. Heat treatment map of Al_2Ca-added AlSi11MnMg pressure-cast alloy plotted by full factorial design of experiment and analysis of variance [J]. Metal Science and Heat Treatment, 2019, 61: 511−516. https://doi.org/ 10.1007/s11041-019-00454-7.

[4] KIM B H, SEYEDSALEHI M, NOURI A, MOHEBBI M S, HA S H, YOON Y O, LIM H K, KIM S K, EISAABADI G. Role of Ca in hot compression behavior and microstructural stability of $AlMg_5$ alloy during homogenization [J]. Transactions of Nonferrous Metals Society of China, 2020, 30: 571−581. https://doi.org/10.1016/S1003-6326(20)65236-0.

[5] SUN Yi-wei. Microstructure evolution in 6XXX and 7XXX aluminum alloys during extrusion and related heat treatments [D]. West Lafayette, Indiana: School of Materials Engineering, Purdue University, 2017.

[6] JIN Neng-ping, ZHANG Hui, HAN Yi, WU Wen-xiang, CHEN Jiang-hua. Hot deformation behavior of 7150 aluminum alloy during compression at elevated temperature [J]. Materials Characterization, 2009, 60: 530−536. https://doi.org/10.1016/j.matchar.2008.12.012.

[7] WEI Li-li, PAN Qin-glin, ZHOU Jian, JIA Ke, YIN Zhi-min. Processing maps and flow instability analysis of Al−Zn−Mg−Cu−Zr alloy [J]. Journal of Central South University (Science and Technology), 2013, 44: 1798−1804. (in Chinese)

[8] HU Hui-e, ZHEN Liang, YANG Li, SHAO Wen-zhou, ZHANG Bao-you. Deformation behavior and microstructure evolution of 7050 aluminum alloy during high temperature deformation [J]. Materials Science and Engineering A, 2008, 488: 64−71. https://doi.org/10.1016/j.msea.2007.10.051.

[9] XU Qing-jun, ZHANG Zhi-min, YANG Yong-biao. Study on thermal deformation performance of 7075 alloy [J]. Hot Working Technology, 2012, 7: 33−35.

[10] HE Jian-liang, ZHANG Da-tong, ZHANG Wei-wen, QIU Cheng, ZHANG Wen. Constitutive equation and hot compression deformation behavior of homogenized Al−7.5Zn−1.5Mg−0.2Cu−0.2Zr alloy [J]. Materials, 2017, 10: 1193. https://doi.org/10.3390/ma10101193.

[11] LENG Jin-feng, REN Bing-hui, ZHOU Qing-bo, ZHAO Ji-wei. Effect of Sc and Zr on recrystallization behavior of 7075 aluminum alloy [J]. Transactions of Nonferrous Metals Society of China, 2021, 31: 2545−2557. https://doi.org/10.1016/S1003-6326(21)65674-1.

[12] LIX Yuan-yuan, ZHENG Xiao-ping, ZHANG Wei-wen, LUO Zong-qiang. Effect of deformation temperature on microstructures and properties of 7075/6009 alloy [J]. Transactions of Nonferrous Metals Society of China, 2009, 19: 1037−1043. https://doi.org/10.1016/S1003-6326(08)60403-3.

[13] WEI Li-li, PAN Qin-glin, ZHOU Jian, JIA Ke, YIN Zhi-min. Processing maps and flow instability analysis of Al−Zn−Mg−Cu−Zr alloy [J]. Journal of Central South University (Science and Technology), 2013, 44: 1798−1804. (in Chinese)

[14] SAKAI T, TAKAHASHI C. Flow softening of 7075 aluminum alloy under hot compression [J]. Materials Transactions−The Japan Institute of Metals, 1991, 32: 375−382. https://doi.org/10.2320/matertrans1989.32.375.

[15] SITDIKOV O S, SAKAI T, GOLOBORODKO A, MIURA H. Grain fragmentation in a coarse-grained 7475 Al alloy during hot deformation [J]. Scripta Materialia, 2004, 51: 175−179. https://doi.org/ 10.1016/j.scriptamat.2004.02.034.

[16] CERRI E, EVANGELISTA E, FORCELLESE A, McQUEEN H. Comparative hot workability of 7012 and 7075 alloys after different pretreatments [J]. Materials Science and Engineering A, 1995, 197: 181−198. https://doi.org/10.1016/0921-5093(94)09714-3.

[17] LU Jue, SONG Yan-li, HUA Lin, ZHENG Kai-lun, DAI Ding-guo. Thermal deformation behavior and processing maps of 7075 aluminum alloy sheet based on isothermal uniaxial tensile tests [J]. Journal of Alloys and Compounds, 2018, 767: 856−869. https://doi.org/10.1016/j.jallcom.2018.07.173.

[18] YANG Yong-biao, XIE Zhi-ping, ZHANG Zhimin, LI Xu-bin, WANG Qiang, ZHANG Yan-hui. Processing maps for hot deformation of the extruded 7075 aluminum alloy bar: Anisotropy of hot workability [J]. Materials Science and Engineering A, 2014, 615: 183−190. https://doi.org/10.1016/j.msea.2014.07.072.

[19] LIANG Zou, PAN Qing-lin, HE Yun-bin, WANG Chang-zhen, LIANG Wen-jie. Effect of minor Sc and Zr addition on microstructures and mechanical properties of Al−Zn−Mg−Cu alloys [J]. Transactions of Nonferrous Metals Society of China, 2007, 17: 340−345. https://doi.org/10.1016/S1003-6326(07)60095-8.

[20] LIU Jing, YAO Pei, ZHAO Nai-qin, SHI Chun-sheng, LI Huijun, LI Xuan, XI De-sheng, YANG Shuo. Effect of minor Sc and Zr on recrystallization behavior and

mechanical properties of novel Al−Zn−Mg−Cu alloys [J]. Journal of Alloys and Compounds, 2016, 657: 717−725. https://doi.org/10.1016/j.jallcom.2015.10.122.

[21] ZHAO Pi-zhi, TSUCHIDA T. Effect of fabrication conditions and Cr, Zr contents on the grain structure of 7075 and 6061 aluminum alloys [J]. Materials Science and Engineering A, 2009, 499: 78−82. https://doi.org/10.1016/j.msea.2007.09.094.

[22] SHI C J, CHEN X G. Hot deformation behavior and microstructural evolution of homogenized 7150 aluminum alloys micro-alloyed with Zr and V [C]//WEILAND H, ROLLETT A D, CASSADA W A. 13th International Conference on Aluminum Alloys (ICAA13). Pittsburgh, 2012: 1599−1605.

[23] KIM B H, SEYEDSALEHI M, KIM S K, MOHEBBI M S, EISAABADI G. Microstructural evolutions of newly developed ECO-7175 aluminum alloy during hot compression: The effect of cr elimination [J]. Materials Science and Engineering A, 2020, 792: 139830. https://doi.org/10.1016/j.msea.2020.139830.

[24] VU C, WERN C, KIM B H, KIM S K, CHOI H J, YI S. Fatigue characteristic analysis of new ECO7175v1 extruded aluminum alloy [J]. Journal of Aerospace Engineering, 2019, 32: 04018128. https://doi.org/10.1061/(ASCE)AS.1943-5525.0000958.

[25] MIAO J S, SUTTON S, LUO A. Microstructure and hot deformation behavior of a new aluminum–lithium–copper based AA2070 alloy [J]. Materials Science and Engineering A, 2020, 777: 139048. https://doi.org/10.1016/j.msea.2020.139048.

[26] HUANG K, MARTINSEN K, ZHAO Q L, LOGÉ R. The double-edge effect of second-phase particles on the recrystallization behaviour and associated mechanical properties of metallic materials [J]. Progress in Materials Science, 2018, 92: 284−359. https://doi.org/10.1016/j.pmatsci.2017.10.004.

[27] HUANG K, LOGÉ R. A review of dynamic recrystallization phenomena in metallic materials [J]. Materials & Design, 2016, 111: 548−574. https://doi.org/10.1016/j.matdes.2016.09.012.

[28] McQUEEN H. Development of dynamic recrystallization theory [J]. Materials Science and Engineering A, 2004, 387−389: 203−208. https://doi.org/10.1016/j.msea.2004.01.064.

[29] LIN Yong-cheng, LIA Lei-ting, XIA Yu-chi, JIANG Yu-qiang. Hot deformation and processing map of a typical Al−Zn−Mg−Cu alloy [J]. Journal of Alloys and Compounds, 2013, 550: 438−445. https://doi.org/10.1016/j.jallcom.2012.10.114.

[30] PENG Xiao-yan, SU Wu-sen, XIAO Dan, XU Guo-fu. Investigation on hot workability of homogenized Al−Zn−Mg−Cu alloy based on activation energy and processing map [J]. The Journal of the Minerals, Metals & Materials Society (JOM), 2018, 70: 993−999. https://doi.org/10.1007/s11837-017-2708-9.

[31] ROKNI M R, ZAREIHANZAKI A, ROOSTAEI A, ABEDI H R. An investigation into the hot deformation characteristics of 7075 aluminum alloy [J]. Materials & Design, 2011, 32: 2339−2344. https://doi.org/10.1016/j.matdes.2010.12.047.

[32] HUMPHREYS F J, HATHERL M. Recrystallization and related annealing phenomena [M]. 2nd ed. Oxford: Elsevier, 2012.

[33] LEE S Y, JUNG T K, SON H W, KIM S W, SON K T, CHOI H J, OH S H, LEE J W, HYUN S K. Hot deformation behavior of hot-extruded AA7175 through hot torsion tests [J]. Journal of Nanoscience and Nanotechnology, 2018, 18: 2144−2147. https://doi.org/10.1166/jnn.2018.14988.

[34] LI Wei-shu, LIU Yao-qiong, JIANG Shuai, LUAN Qin-meng, LI Yibo, GU Bin, SHI Zhu-sheng. A study of thermomechanical behaviour and grain size evolution of AA7050 under hot forging conditions [J]. International Journal of Lightweight Materials and Manufacture, 2019, 2: 31−39. https://doi.org/10.1016/j.ijlmm.2018.10.002.

[35] MURRAY J L. The Al−Cr (aluminum−chromium) system [J]. Journal of Phase Equilibria, 1998, 19: 367.

[36] SELLARS C M, McTEGART W J. On the mechanism of hot deformation [J]. Acta Metallurgica, 1966, 14: 136−138. https://doi.org/10.1016/0001-6160(66)90207-0.

[37] DAI Qing-song, DENG Yun-lai, TANG Jian-guo, WANG Yu. Deformation characteristics and strain-compensated constitutive equation for AA5083 aluminum alloy under hot compression [J]. Transactions of Nonferrous Metals Society of China, 2019, 29: 2252−2261. https://doi.org/10.1016/S1003-6326(19)65131-9.

[38] HE Jun-guang, WENA Jiu-ba, ZHOU Xu-dong, LIU Yang-yang. Hot deformation behavior and processing map of cast 5052 aluminum alloy [J]. Procedia Manufacturing, 2019, 37: 2−7. https://doi.org/10.1016/j.promfg.2019.12.003.

[39] LIU Jun-wei, ZHAO Zhi-gang, LU Shi-qiang. Microstructure evolution and constitutive equation for the hot deformation of LZ91 Mg alloy [J]. Catalysis Today, 2018, 318: 119−125. https://doi.org/10.1016/j.cattod.2017.10.019.

[40] LIU Jian-jun, WANG Kelu, LU Shi-qiang, GAO Xia-yun, LI Xin, ZHOU Feng. Hot deformation behavior and processing map of Zr-4 alloy [J]. Journal of Nuclear Materials, 2020, 531: 151993. https://doi.org/10.1016/j.jnucmat.2020.151993.

[41] ZHANG Ming-jie, LI Fu-guo, WANG Shu-yun, LIU Chen-yi. Characterization of hot deformation behavior of a P/M nickel-base superalloy using processing map and activation energy [J]. Materials Science and Engineering A, 2010, 527: 6771−6779. https://doi.org/10.1016/j.msea.2010.07.039.

[42] SANI S A, EBRAHIMI G R, VAFAEENEZHAD H, KIANIRASHID A R. Modeling of hot deformation behavior and prediction of flow stress in a magnesium alloy using constitutive equation and artificial neural network (ANN) model [J]. Journal of Magnesium and Alloys, 2018, 6: 134−144. https://doi.org/ 10.1016/j.jma.2018.05.002.

[43] SHI C J, MAO Wei-ming, CHEN X G. Evolution of activation energy during hot deformation of AA7150 aluminum alloy [J]. Materials Science and Engineering A, 2013, 571: 83−91. https://doi.org/10.1016/j.msea.2013.01.080.

[44] SHI Cang-ji, CHEN Xiao-grant. Evolution of activation energies for hot deformation of 7150 aluminum alloys with various Zr and V additions [J]. Materials Science and

Engineering A, 2016, 650: 197−209. https://doi.org/10.1016/j.msea.2015.09.105.

[45] WANG Shuai, HOU Long-gang, LUO Jin-ru, ZHANG Ji-shan, ZHUANG Lin-zhong. Characterization of hot workability in AA 7050 aluminum alloy using activation energy and 3-D processing map [J]. Journal of Materials Processing Technology, 2015, 225: 110−121. https://doi.org/10.1016/j.jmatprotec.2015.05.018.

[46] WANG Zhen-jun, QI Le-hua, GUI Wang, LI He-jun, DARGUSCH M S. Constitutive equation for the hot deformation behavior of Csf/AZ91D composites and its validity for numerical simulation [J]. Mechanics of Materials, 2016, 102: 90−96. https://doi.org/10.1016/j.mechmat.2016.08.011.

[47] SIMONOVIC D, SLUITER M. Impurity diffusion activation energies in Al from first principles [J]. Physical Review B, 2009, 79: 054304. https://doi.org/10.1103/PhysRevB.79.054304.

[48] BÄCKE L. Modeling the effect of solute drag on recovery and recrystallization during hot deformation of Nb microalloyed steels [J]. ISIJ International, 2010, 50: 239−247. https://doi.org/10.2355/isijinternational.50.239.

[49] KAPOOR R, CHAKRAVARTTY J. Deformation behavior of an ultrafine-grained Al–Mg alloy produced by equal-channel angular pressing [J]. Acta Materialia, 2007, 55: 5408−5418. https://doi.org/10.1016/ j.actamat.2007.05.049.

[50] BUKEN H, KOZESCHNIK E. A model for static recrystallization with simultaneous precipitation and solute drag [J]. Metallurgical and Materials Transactions A, 2017, 48: 2812−2818. https://doi.org/10.1007/s11661-016-3524-5.

[51] CAHN J W. The impurity-drag effect in grain boundary motion [J]. Acta Metallurgica, 1962, 10: 789−798. https://doi.org/10.1016/0001-6160(62)90092-5.

[52] KOJU R K, MISHIN Y. The role of grain boundary diffusion in the solute drag effect [J]. Nanomaterials, 2021, 11: 2348. https://doi.org/10.3390/nano11092348.

[53] HERSENT E, MARTHINSEN K, NES E. The effect of solute atoms on grain boundary migration: A solute pinning approach [J]. Metallurgical and Materials Transactions A, 2013, 44: 3364−3375. https://doi.org/10. 1007/s11661-013-1690-2.

[54] DU Yong, CHANG A, HUANG Bai-yun, GONG Wei-ping, JIN Zhan-peng, XU Hong-hui, YUAN Zhao-hui, LIU Yong, HE Yue-hui, XIE Fan-you. Diffusion coefficients of some solutes in FCC Al and liquid Al: critical evaluation and correlation [J]. Materials Science and Engineering A, 2003, 363: 140−151. https://doi.org/10.1016/S0921-5093(03)00624-5.

[55] PRASAD Y V R K, GEGEL H, DORAIVELU S, MALAS J, MORGAN J, LARK K A, BARKER D R. Modeling of dynamic material behavior in hot deformation: Forging of Ti-6242 [J]. Metallurgical Transactions A, 1984, 15: 1883−1892. https://doi.org/ 10.1007/BF02664902.

[56] ZIEGLER H. An introduction to thermomechanics [M]. Amsterdam: North-Holland Publishing Company, 1983.

[57] SESHACHARYULU T, MEDEIROS S, FRAZIER W G, PRASAD Y V R K. Hot working of commercial Ti−6Al−4V with an equiaxed α−β microstructure: Materials modeling considerations [J]. Materials Science and Engineering A, 2000, 284: 184−194. https://doi.org/10.1016/S0921-5093(00)00741-3.

[58] YANG J Y, KIM W J. The effect of addition of Sn to copper on hot compressive deformation mechanisms, micro-structural evolution and processing maps [J]. Journal of Materials Research and Technology, 2020, 9: 749−761. https://doi.org/10.1016/j.jmrt.2019.11.015.

[59] PRASAD Y V R K. Recent advances in the science of mechanical processing [J]. Indian Journal of Technology, 1990, 28: 435−451.

[60] GUO Liang-gang, YANG Shuang, YANG He, ZHANG Jun. Processing map of as-cast 7075 aluminum alloy for hot working [J]. Chinese Journal of Aeronautics, 2015, 28: 1774−1783. https://doi.org/10.1016/j.cja.2015.08.002.

[61] MOMENI A, DEHGHANI K, EBRAHIMI G. Modeling the initiation of dynamic recrystallization using a dynamic recovery model [J]. Journal of Alloys and Compounds, 2011, 509: 9387−9393. https://doi.org/10.1016/j.jallcom.2011.07.014.

[62] LI Peng-wei, LI Hui-zhong, HUANG Lan, LIANG Xiao-peng, ZHU Ze-xiao. Characterization of hot deformation behavior of AA2014 forging aluminum alloy using processing map [J]. Transactions of Nonferrous Metals Society of China, 2017, 27: 1677−1688. https://doi.org/10.1016/S1003-6326(17)60190-0.

[63] ZHEN Liang, HU Hui-e, WANG Xin-yun, ZHANG Bao-you, SHAO Wen-zhu. Distribution characterization of boundary misorientation angle of 7050 aluminum alloy after high temperature compression [J]. Journal of Materials Processing Technology, 2009, 209: 754−761. https://doi.org/10.1016/j.jmatprotec.2008.02.042.

[64] JEONG H J, KIM W J. Comparison of hot deformation behavior characteristics between as-cast and extruded Al−Zn−Mg−Cu (7075) aluminum alloys with a similar grain size [J]. Materials, 2019, 12: 3807. https://doi.org/10.3390/ma12233807.

[65] ALDER P, DEIASI D. Calorimetric studies of 7000 series aluminum alloys: II. Comparison of 7075, 7050, and RX720 alloys [J]. Metallurgical and Materials Transactions A, 1997, 8: 1185−1190. https://doi.org/10.1007/ BF02667404.

[66] LIN Yong-cheng, JIANG Yu-qiang, CHEN Xiao-min, WEN Dong-xu, ZHOU Hua-min. Effect of creep-aging on precipitates of 7075 aluminum alloy [J]. Materials Science and Engineering A, 2013, 588: 347−356. https://doi.org/10.1016/j.msea.2013.09.045.

[67] STARINK M, MILKEREIT M, ZHANG Yong, ROMETSCH P. Predicting the quench sensitivity of Al−Zn−Mg−Cu alloys: A model for linear cooling and strengthening [J]. Materials & Design, 2015, 88: 958−971. https://doi.org/10.1016/j.matdes.2015.09.058.

Cr 对 ECO-7175 铝合金热压过程中流变行为和加工图的影响

Majid SEYED-SALEHI[1], Bong Hwan KIM[2], Seung Yoon YANG[2,3],
Shae Kwang KIM[2], Ghasem EISAABADI BOZCHALOEI[4]

1. Faculty of Materials Science and Engineering, K. N. Toosi University of Technology, 1969764499, Tehran, Iran;
2. Korea Institute of Industrial Technology, 7-47 Songdo-dong, Incheon 406-840, Korea;
3. Department of Advanced Materials Science and Engineering, Sungkyunkwan University, Suwon 16419, Korea;
4. Department of Materials Science and Engineering, Faculty of Engineering, Arak University, 3813853945, Arak, Iran

摘　要：研究 Cr 元素对新开发的 ECO-7175 合金热变形行为的影响。采用 Gleeble 热模拟机对含 Cr 和不含 Cr 的 ECO-7175 样品进行热压(温度为 350~500 ˚C、应变速率为 0.001~1 s^{-1})，研究合金的本构方程、加工图和显微组织演变。对变形激活能的分析表明，含 Cr 合金中速率控制变形机制由 Al 的自扩散(或 Al 中 Mg 的扩散)逐渐转变为 Al 中 Cr 的扩散，且 Zener−Hollomon 参数减小。对含 Cr 合金的加工图的分析表明， 动态再结晶(DRX)区局限于高温和低应变速率下的变形，且随着应变的增加而扩大。 另一方面，发现 Al 的自扩散(或 Al 中 Mg 的扩散)是无铬合金在所有加工条件下热变形过程中唯一的速率控制机制，其 DRX 区与塑性应变无关。

关键词：热变形；本构方程；加工图；ECO-7175 铝合金

(Edited by Bing YANG)